Calibration and Characterisation of Microwave Sounders With the Moon

M. J. Burgdorf[1], S. A. Buehler[1], M. Prange[1]

[1] Universität Hamburg, Faculty of Mathematics, Informatics and Natural Sciences, Department of Earth Sciences, Meteorological Institute, Bundesstraße 55, 20146 Hamburg, Germany

Key Points:

- The quasi-optical components of microwave sounders were characterized with appearances of the Moon.
- The disk-integrated brightness temperature of the Moon was measured for perihelion and aphelion.
- Two different models of the lunar radiance were put to the test.

Corresponding author: M. J. Burgdorf, martin.burgdorf@uni-hamburg.de

Abstract

A major problem with calculating the uncertainties of measurements with weather satellites is the fact that a full characterisation and calibration of their instruments can only be carried out before launch. The Moon, however, makes at least some of these activities possible in flight as well by providing a reliable flux reference at a well-defined position. We used serendipitous observations of the Moon with AMSU-B and MHS on eight different satellites to measure pointing accuracy, spectral channels coregistration, and beamwidth with unprecedented accuracy in flight. In addition we compared these findings with the corresponding values obtained on ground. By analysing more than a hundred Moon intrusions in the deep space view we could determine the radiance of the Moon as a function of its phase angle and distance from the Sun. The difference in average brightness temperature of the lunar disk between perihelion and aphelion amounts to 4.4 ± 2.3 K at 183 GHz. We compare the measured brightness temperature of the Moon as a function of phase angle between −85° (waxing) and +76° (waning) with the predictions from two models and find that one of them reproduces the shape of this function very well.

1 Introduction

A fundamental problem with scientific instruments on space platforms is the detection and characterisation of changes in performance during the mission. It stems from the fact that they usually cannot be brought back to Earth and tested under controlled conditions and against SI-traceable standards. This issue is particularly serious in cases, where small variations need to be detected on long time scales, like for example in studies of how essential climate variables change. Systematic effects can cause a slow deterioration of the flux calibration, e. g. changes in the reflectivity of a solar diffusor or in the resistance of a temperature sensor. In such cases it is helpful to have a reference, whose flux can be accurately predicted and that never shows signs of wear or weathering. In case of meteorological research satellites the Moon has been identified as such an object for instruments operating in the visible, near and shortwave infrared spectral ranges (Kieffer et al., 2003). A reliable spectral radiance model, to which the spacecraft observations of the Moon are compared, is essential, because the lunar flux varies with wavelength, phase angle, distance, etc. Such models are available for calibration at wavelengths dominated by reflected sunlight (Kieffer & Stone, 2005; Stone, 2010; Kouyama et al., 2016), but the uncertainties of similar models in the microwave range were too large. They amount to several percent for the specific intensity I_ν at frequency ν or more (Krotikov & Pelyushenko, 1987), and yet they are still being used for the calibration of astronomical observatories (Appel et al., 2019).

The measurements of the lunar flux with microwave sounders on weather satellites are plentiful: A few hundred orbits during the lifetime of a satellite are typically affected by serendipitous intrusions of the Moon in the deep space view of a microwave sounder like MHS (Microwave Humidity Sounder, Table 1). If the Moon produces a strong signal in three different pixels, it is possible to calculate an accurate and reliable brightness temperature, T_B, defined by

$$T_B \equiv \frac{c^2}{2k\nu^2} I_\nu, \tag{1}$$

where c is the speed of light and k is Boltzmann's constant. While such serendipitous observations happen with every satellite in a polar orbit, there has recently also been a special spacecraft pitch-manoeuvre operation to observe the full Moon with ATMS (Advanced Technology Microwave Sounder) on NOAA-20 (Yang et al., 2020). This campaign gave accurate values of the Moon's brightness temperature in the frequency range of 23–183 GHz, which are useful to check the results obtained with older satellites - measurements dating back two decades or more. The uncertainties inherent in the models, on the other hand, become apparent in the different predictions made by the two exemplars

we chose for comparison with measurements of the lunar radiance with MHS. One is the model by Keihm (1984), which is based on data from the Apollo heat flow experiment and the thermophysical and electrical properties of Apollo samples. The other is by Liu and Jin (2020) and relies mainly on the results from remote sensing in the infrared and microwave range with spacecrafts in orbits around the Moon.

Table 1. Microwave Humidity Sounder (MHS) - Channels and Passband Characteristics

Channel No.	Central Freq. (GHz)	Bandwidth (MHz)	No. of Passbands
H1	89	2800	1
H2	157	2800	1
H3	183.3 ± 1	1000	2
H4	183.3 ± 3	2000	2
H5	190.3	2000	1

Even when a thermo-physical model of the Moon is wrong in the sense that it cannot correctly reproduce its absolute radiance, it can still be useful for checking the stability of flux calibration, because the detection of small changes is here more important than the accuracy of the absolute flux level. Therefore the model only needs to provide the exact corrections that have to be applied for making observations of the Moon comparable that were taken at different phase angles, distances from Earth and Sun, etc. When MHS on satellites from the Metop (Meteorological operational satellite) series, for example, observes a chance intrusion of the Moon in its deep space view, it can only do so with phase angles in an interval of some 30°. This is so, because all Metop satellites have the same, constant equator crossing time. Hence any requirements on the numerical simulation of the brightness temperature of the Moon have to be carefully adjusted to the peculiarities of the observational data base.

The work we describe in this article was carried out with the aim to find out, whether a new model of the disk-integrated flux density of the Moon is accurate enough to establish the Moon as calibration reference source for microwave sounders. We focused our attention on two aspects: changes in phase angle and changes in the distance between the Sun and the Moon. If the angular diameter of a target is smaller than the beam of a microwave instrument, as is the case with the Moon, then the resulting signal depends strongly on the distance of the target from the center of the beam. We took advantage of this property to characterise the beams of MHS and AMSU-B (Advanced Microwave Sounding Unit-B, Table 2) on eight different satellites, in addition to their photometric calibration and its uncertainty.

2 Materials and Methods

Most microwave sounders are orbiting the Earth in polar orbits. This means that their Deep Space View (DSV), whose signal serves as cold reference, is always pointed at areas in the sky that are close to the celestial equator. As a consequence the Moon appears sometimes in the DSV and spoils the calibration, because the incoming flux is no longer defined by the cosmic microwave background alone. In order to cope with this nuisance, the programs "mhscl" and "amsubcl" in AAPP (ATOVS [Advanced TIROS-N (Television and Infra-Red Observation Satellite - N) Operational Vertical Sounder] and AVHRR [Advanced Very High Resolution Radiometer] Pre-processing Package) were written. They calculate the distance between the pointing direction of the DSV and the position of the Moon and enable therefore the identification of scans that should not be used in the standard calibration procedure. With the help of these programs we identified Moon

Table 2. Advanced Microwave Sounding Unit-B - Channels and Passband Characteristics

Channel No.	Central Freq. (GHz)	Bandwidth (MHz)	No. of Passbands
16	89	1000	2
17	150	1000	2
18	183.3 ± 1	500	2
19	183.3 ± 3	1000	2
20	183.3 ± 7	2000	2

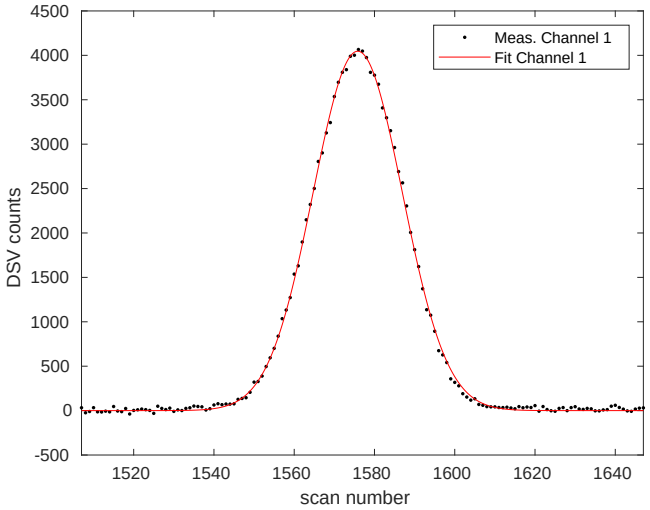

Figure 1. Number of counts from the DSV as a function of scan number during a Moon intrusion. The data were taken with MHS on NOAA-18 on 1/14, 2014, at 7:28 UTC (time of maximum signal). A Gaussian was fitted to the light curve after subtraction of the count level in the absence of the Moon (cosmic microwave background only).

intrusions for AMSU-B and MHS already in the raw data (Level 1b), where the signal is still expressed as digital counts. Plotting the number of counts obtained in the DSV for each channel as a function of time t produces light curves that resemble a Gaussian, see Figure 1. The Gaussian fit provides three parameters: its amplitude a_n, its centroid location b_n, and its peak width c_n. n is the number of a pixel in the DSV; it can take values between one and four. We want to characterise, however, not only the scan number, where the Moon was closest to the pointing direction of the DSV, i. e. b_n, but also the number of the pixel, which came closest to the Moon. This number is in general not an integer: 2.2 means for example that the Moon was closest to pixel 2 and closer to pixel 3 than to pixel 1. Such an accurate determination of the Moon's position in two dimensions was deemed unfeasible in the past. Bonsignori (2017) argued namely that only oversampled measurements (e.g. sampling distance in the order of 0.1°) would give good results, whereas the DSV of AMSU-B and MHS provides only four angular samples spaced by 1.111°. We challenge this assumption. In fact, any sampling distance will do, as long as one gets a good signal-to-noise ratio in at least two samples. If $a_1 = a_3$ or $a_2 = a_4$, then it is certain that the Moon was at the center of pixel 2 or 3, respectively. In the real

world, however, the counts from different pixels are never exactly the same, but similar at best. In order to calculate how similar we want them to be, we assume that the distance between adjacent pixels and the full width at half maximum of the beam (FWHM) amount both to 1.1°, like stated in the specifications of the instruments. A displacement of the Moon by 0.07° from the center of the field of view causes here a loss of signal of only 1%. $\frac{a_1}{a_3}$ or $\frac{a_2}{a_4}$, however, are in this case 0.5 or 2. This huge difference shows that the relative amplitudes of the light curves from the four DSV pixels depend strongly on the position of the Moon in the scan direction. They offer therefore a great way of measuring exactly where the Moon moved between the pixels of the DSV.

We calculated this pixel position by applying another Gaussian fit to the four amplitudes and considered the amplitude of this fit the signal from the Moon intrusion. This second Gaussian fit was applied if and only if the maximum signal was found in pixel 2 or 3, because in this case we can be sure that at the most one pixel did not receive any flux from the Moon. Our four flux values from the four DSV pixels are enough to calculate the three parameters that define a Gaussian. One of them is the centroid location, but unlike the centroid location from the fit to the light curves it does not correspond to the scan number but to the pixel position of maximum signal. The previously calculated scan number describes the component of the pointing in the along track direction, and the pixel position describes the component of the pointing in the across track, i. e. scan, direction (Bonsignori, 2017).

Another important property of a microwave sounder that can be determined from the Gaussian fit to the light curve of a Moon intrusion is the mean half power beamwidth. During ground tests it is possible to characterise the beam pattern in two dimensions by moving a source of radiation in different directions through the beam of the microwave sounder. With the Moon, however, we get only information about the shape of the beam in two directions: along and across track. With only four pixels available to determine the peak width c_n of the Gaussian fit in the across track direction, but with many scans available to determine the peak width in the along track direction, see Figure 1, we calculated only the latter. Another reason for excluding the peak width in the across track direction from our considerations is the fact that the scan velocity profile is not constant (Robel & Graumann, 2014). It is therefore subject to larger uncertainties than the unchanging orbital velocity of the satellite. With other words, the distance between two pixels of the DSV might differ from the nominal value of 1.1°. Hence we have to assume in the following that the beam is rotationally symmetric with an FWHM proportional to c_{n_0}, n_0 being the number of the pixel coming closest to the Moon. It has the strongest signal and therefore the best signal-to-noise ratio.

The exact FWHM of the beam is essential for our last processing step, viz. calculating the flux received from the Moon. As we started with raw data, we cannot rely on the pipeline processing for the conversion from counts to physical quantities. We converted instead the counts from each space view and every channel to brightness temperatures by interpolating between the signal obtained from the DSV in the absence of the Moon and the internal calibration source (ICS). In order to obtain the average brightness temperature of the lunar disk, one has to take into consideration that the FWHM of the beam is more than double the diameter of the Moon, whereas the ICS covers the complete diameter of the beam. Even the side lobes receive much more flux, when the instrument is pointed at the built-in black body, than they get from deep space around the Moon. These effects are included in our calibration procedure for AMSU-B and MHS as described in Yang and Burgdorf (2020). The conversion from c_n to FWHM in degrees follows the method described in Burgdorf et al. (2019); it is basically the product of the duration of the Moon intrusion and the angular velocity of the pointing direction of the DSV.

3 Data

Our data processing started with the complete set of Level 1b Records of AMSU-B and MHS that we obtained from NOAA via CLASS (Comprehensive Large Array-data Stewardship System). First we identified the date and approximate time of the intrusions of the Moon in the DSV and as well the names of the files affected by such events. The processing of these raw data produced in the above-mentioned way a data set with the signal counts, the number of pixel and scan, where the signal reached its maximum value, and the beam width for each lunar intrusion in the DSV that we have analyzed. From the longitude and latitude of the pixel closest to nadir and the height of the satellite above the ground we could determine the phase angle and the equatorial angular width of the full lunar disk, if it were fully illuminated. This information is then used to calculate the disk-integrated brightness temperature of the Moon, the date and exact time of its intrusion in the DSV, and its distance from the Sun.

4 Results

We present in the following the results obtained with the methods described in Section 2. In doing so we build up the knowledge about the characteristics of the instruments that is necessary for measuring the brightness temperature of the Moon and its dependence on phase angle and solar distance with sufficient accuracy to assess the validity of models.

4.1 Spectral Channels Co-Registration

Bonsignori (2017) developed a method for calculating the channel co-registration in the along track direction. It can be used as well, however, for measuring the channel co-registration in the perpendicular direction, i.e. across track, by comparing the signal in the different space view pixels for each channel, see Section 2.

Our efforts went beyond a determination of the channel co-registration in both along and across track direction: We wanted to check also the absolute pointing accuracy of AMSU-B and MHS. Therefore we only considered cases, in which the Moon came closer than 0.05° to the center of the deep space view according to the pointing information in the Level 1b Records and the programs "mhscl" and "amsubcl" in AAPP. The error in the calculated pointing direction of the instrument is at worst 0.3°, according to EUMETSAT (2013), but in most cases much better (Burgdorf et al., 2016). Nevertheless it is the largest source of uncertainty in the determination of the absolute pointing accuracy. As it is a random effect, however, it can be reduced by using a large number of measurements. Hence we identified more than thirteen of such cases for each satellite, except for Metop-C, which was launched later than the others. The errors in the pointing of the satellite calculated with AAPP cancelled then out to a large extent in the mean of all Moon intrusions we considered, and the uncertainty of the mean of all pointings was smaller than 0.05° for all instruments, again except for Metop-C. (We mention here in passing that by averaging the pointing errors of many observations we eliminated several sources of geolocation errors discussed by Moradi et al. (2013) so that their results are not directly comparable to ours.) This uncertainty might contain a contribution caused by systematic changes of the pointing error with time. With the number of measurements we had available, however, it was not possible to find any significant correlation between pointing error and time. Therefore we conclude that any time dependency of the pointing error must be rather small, if it exists at all. In any case the absolute pointing error of the microwave sounders in our study was in most cases much larger than the uncertainty of our measurements. The results are shown in Figure 2, and the exact numbers with one-σ uncertainties are listed in Table 3. We follow the naming convention by Ackermann (2018), i. e. ϕ is the azimuth (across track direction) and θ is the elevation (approximately along track direction), with the exception of the origin for both angles being the nominal view

as given in the Level 1b Records. The nominal beam pointing accuracy is ± 0.01° for either axis of AMSU-B (Robel & Graumann, 2014) and ± 0.009° (± 0.012° overall pointing budget) for MHS (Costes, 1999). The antenna requirement for channels coregistration is ± 0.007° for MHS. When errors are more than twice the value allowed by the requirements they are printed in boldface in Table 3.

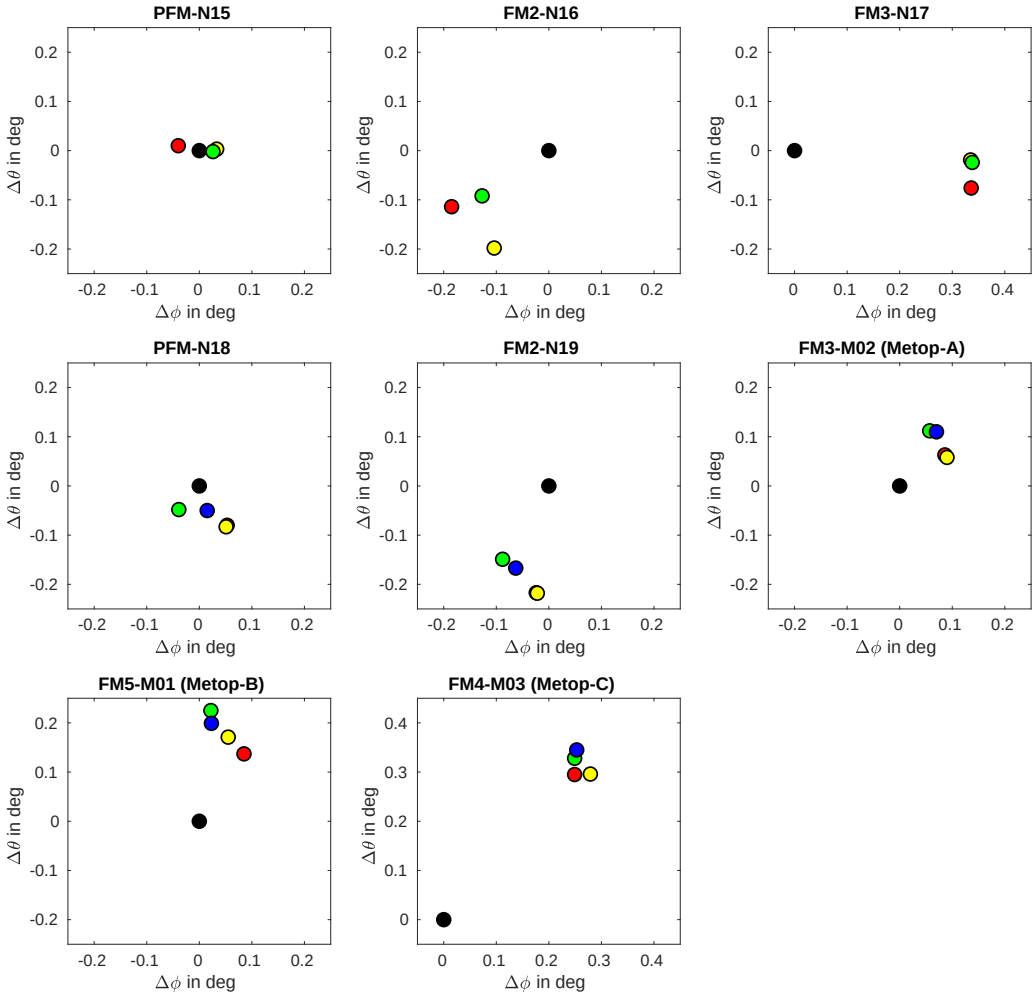

Figure 2. In-flight pointing performance showing the coregistration of the channels 16/H1 (red), 17/H2 (yellow), 18-20/H3-4 (green, only channel H4 with NOAA-19 because of the poor signal-to-noise ratio of channel H3), and H5 (blue) at the space view. $\Delta\phi$ is the error in across track direction, $\Delta\theta$ is the error in along track direction. The black circle indicates the nominal pointing direction; yellow is sometimes on top of red and green on top of yellow. 0.1° equals 1.745 mrad in angle and corresponds to some 1.5 km at the sub satellite point. This means that the largest displacement is approximately a third of a pixel.

Table 3. Pointing Accuracy and Co-Alignment: Δ is the difference between the measured position of the Moon relative to the DSV and the prediction by AAPP, based on the pointing information in the Level 1b Records for a given channel. The subscript "gr" indicates values obtained during ground tests (where of course a test range was used instead of the Moon), the subscript "op" indicates values obtained during the operational phase of the satellite. "Error" is the difference between nominal and actual pointing direction, i. e. $\sqrt{(\Delta\phi_{op})^2 + (\Delta\theta_{op})^2}$. The difference between two channel numbers indicates the coregistration of the window channels, i.e. the difference of their Δ values.

Satellite	Channel	$\Delta\phi_{gr}$ (deg)	$\Delta\phi_{op}$ (deg)	$\Delta\theta_{gr}$ (deg)	$\Delta\theta_{op}$ (deg)	Error (deg)
NOAA-15	16		-0.04 ± 0.025		0.010 ± 0.029	0.04
NOAA-15	17		0.033 ± 0.023		0.003 ± 0.027	0.03
NOAA-15	18/19/20		0.026 ± 0.014		-0.002 ± 0.017	0.03
NOAA-15	17 - 16		0.073 ± 0.011		-0.006 ± 0.004	
NOAA-16	16		-0.185 ± 0.036		-0.114 ± 0.032	0.22
NOAA-16	17		-0.104 ± 0.033		-0.198 ± 0.033	0.22
NOAA-16	18/19/20		-0.127 ± 0.020		-0.092 ± 0.019	0.16
NOAA-16	17 - 16		0.081 ± 0.014		-0.084 ± 0.002	
NOAA-17	16		$\mathbf{0.336 \pm 0.023}$		-0.076 ± 0.044	**0.34**
NOAA-17	17		$\mathbf{0.335 \pm 0.021}$		-0.019 ± 0.047	**0.34**
NOAA-17	18/19/20		$\mathbf{0.338 \pm 0.011}$		-0.024 ± 0.028	**0.34**
NOAA-17	17 - 16		-0.001 ± 0.019		0.057 ± 0.008	
NOAA-18	H1	-0.04	0.053 ± 0.022	0.16	-0.080 ± 0.045	0.10
NOAA-18	H2	-0.02	0.051 ± 0.034	0.18	-0.083 ± 0.045	0.10
NOAA-18	H34	-0.12	-0.039 ± 0.021	0.18	-0.048 ± 0.032	0.06
NOAA-18	H5	-0.03	0.015 ± 0.030	0.19	-0.050 ± 0.043	0.05
NOAA-18	H2 - H1	0.02	-0.002 ± 0.005	0.02	-0.003 ± 0.003	
NOAA-19	H1	-0.15	-0.024 ± 0.022	0.01	$\mathbf{-0.217 \pm 0.025}$	0.22
NOAA-19	H2	-0.16	-0.022 ± 0.024	-0.01	$\mathbf{-0.218 \pm 0.023}$	0.22
NOAA-19	H4	-0.21	-0.088 ± 0.020	0.00	-0.149 ± 0.020	0.17
NOAA-19	H5	-0.20	-0.063 ± 0.022	0.02	-0.167 ± 0.022	0.18
NOAA-19	H2 - H1	-0.01	0.002 ± 0.003	-0.02	-0.001 ± 0.004	
Metop-A	H1	0.01	0.086 ± 0.030	0.12	0.063 ± 0.022	0.11
Metop-A	H2	0.00	0.090 ± 0.030	0.13	0.058 ± 0.021	0.11
Metop-A	H34	0.04	0.057 ± 0.021	0.15	0.112 ± 0.018	0.13
Metop-A	H5	0.05	0.070 ± 0.028	0.15	0.110 ± 0.024	0.13
Metop-A	H2 - H1	-0.01	0.004 ± 0.009	0.00	-0.004 ± 0.009	
Metop-B	H1	-0.04	0.085 ± 0.026	0.28	0.137 ± 0.033	0.16
Metop-B	H2	-0.05	0.055 ± 0.026	0.28	0.171 ± 0.035	0.18
Metop-B	H34	-0.09	0.022 ± 0.017	0.33	$\mathbf{0.225 \pm 0.026}$	0.23
Metop-B	H5	-0.08	0.023 ± 0.025	0.31	$\mathbf{0.199 \pm 0.036}$	0.20
Metop-B	H2 - H1	-0.01	-0.030 ± 0.004	0.00	0.035 ± 0.004	
Metop-C	H1	0.07	$\mathbf{0.249 \pm 0.054}$	0.14	$\mathbf{0.295 \pm 0.049}$	**0.39**
Metop-C	H2	0.12	$\mathbf{0.279 \pm 0.046}$	0.14	$\mathbf{0.296 \pm 0.049}$	**0.41**
Metop-C	H34	0.14	$\mathbf{0.249 \pm 0.040}$	0.15	$\mathbf{0.328 \pm 0.038}$	**0.41**
Metop-C	H5	0.13	$\mathbf{0.253 \pm 0.077}$	0.15	$\mathbf{0.345 \pm 0.057}$	**0.43**
Metop-C	H2 - H1	0.05	0.03 ± 0.014	0.05	0.001 ± 0.001	

4.2 Mean Half Power Beamwidth

Just as we calculated the position of the beam axis in the along track direction from the exact timing of the maximum signal of the light curve during an intrusion of the Moon in the deep space view, we can determine the beamwidth from the period of time that the signal stays above half the maximum value. The fact that the Moon is an extended source, however, causes a broadening of the light curve compared to its shape for a hypothetical point source. We take this effect into account by subtracting 0.02° from the FWHM. This value was found by Xu et al. (2020) from deconvolution of the observations of the Moon with the Cosmology Large Angular Scale Surveyor, a ground-based telescope array that observes at 40, 90, 150, and 220 GHz with beams having a FWHM of 1.5°, i. e. slightly larger than the instantaneous field of view of AMSU-B and MHS. The results from our investigation are summarized in Table 4. The requirement for beamwidth is 1.1° ± 0.11° for AMSU-B (Robel & Graumann, 2014) and MHS (Costes, 1999). When the beamwidths are significantly larger than 1.21°, i. e. outside the amount allowed by the requirement, they are printed in boldface.

4.3 Brightness Temperature of the Moon at Perihelion and Aphelion

The equatorial angular width of the Moon full disk and the mean half power beam width of the microwave sounders are needed to convert the flux density received from the Moon to brightness temperature (Yang & Burgdorf, 2020). With the findings from the previous section we are now in the position to use the third parameter from the Gaussian fits to the light curves, viz. their amplitude, to see how the brightness temperature, averaged over the lunar disk, depends on the phase angle. As the observations of the Moon with MHS on NOAA-18 covered the range from first quarter to full Moon almost completely, this satellite is particularly well suited for this purpose. In order to take full advantage of the range of available phase angles, we calculated the brightness temperature T_B for each Moon intrusion of this satellite. All of these intrusions happened at different phases of the Moon, and we fitted then a fifth order polynomial to T_B as a function of phase angle to the whole set.

In doing so, however, we neglected a subtle effect: As the distance between the Sun and the Moon d_{SM} varies slightly because of the eccentricity of the Earth's orbit, the brightness temperature of the Moon must be lower at aphelion than at perihelion. In order to calculate the size of this effect, we analysed 114 intrusions of the Moon in the DSV of MHS on NOAA-18 and selected those, where the maximum signal of the light curve was similar in the DSV pixels 1 and 3 or 2 and 4, because in these cases the Moon moved right through the center of the pixel in between, see Section 2. In case of channel 1 (89 GHz) we also excluded Moon intrusions, where the uncertainty of the amplitude from the first Gaussian fit, i.e. the one to the light curve, was higher than usual. As this channel has the lowest noise (Hans et al., 2017), a larger uncertainty of the Gaussian fit betrays the presence of small, systematic deviations in the light curve from a Gaussian shape. All light curves in all channels underwent a careful visual inspection, and when unusually large noise or sudden jumps in the signal were found, the affected Moon intrusion was excluded from further processing as well. We identified 47 intrusions of the Moon in the DSV with channel 1, 59 intrusions with channel 2, and 58 intrusions with channels 3 - 5 that fulfilled these conditions of proximity of the Moon to the center of the DSV in combination with a good Gaussian fit to the light curve. Then we calculated for each Moon intrusion the difference of its T_B to the value calculated with the polynomial mentioned above for the corresponding phase angle. With other words, we calculated the deviation of the actually measured T_B from what was expected when d_{SM} was ignored. We found a clear, negative correlation between the brightness temperature of the Moon and its distance from the Sun at all three frequencies after merging the values from channel 5 at 190 GHz with the sounding channels at 183 GHz. This relationship is plain to see in Figure 3, where the data set was smoothed. The data set without smoothing was used to

Table 4. Mean half power beamwidth of AMSU-B on NOAA-15 - NOAA-17 and MHS on NOAA-18, NOAA-19, and Metop from ground tests (subscript "gr"), if published (Hewison, 1993; Costes, 1998, 1999; Costes et al., 1999), and in orbit (subscript "op"). An elevation cut, giving the mean half power beamwidth in the along track direction, is used for calculation, except for the ground tests of MHS, where the average of four cuts in different directions is used. For NOAA-19 we used channel H4 instead of the average of channels H3 and H4 because of the poor signal-to-noise ratio in channel H3. The mean half power beamwidth was determined at the DSV position except for the ground tests of AMSU-B, where it refers to Px 90, i. e. the Earth scene closest to DSV. The large uncertainties of the values for Metop in orbit suggest that these values might be affected by a large systematic uncertainty on top of the random scatter. Probably the assumption of an axisymmetric Gaussian beam pattern is not correct in these cases. All angles are in degrees.

Sat.	$(16/\mathrm{H1})_{gr}$	$(16/\mathrm{H1})_{op}$	$(17/\mathrm{H2})_{gr}$	$(17/\mathrm{H2})_{op}$	$(18-20/\mathrm{H3}-4)_{gr}$	$(18-20/\mathrm{H3}-4)_{op}$	$\mathrm{H5}_{gr}$	$\mathrm{H5}_{op}$
N15	1.12	1.199 ± 0.005	1.03	$\mathbf{1.293 \pm 0.011}$	1.05	1.207 ± 0.006		
N16	1.12	1.212 ± 0.006	1.05	$\mathbf{1.338 \pm 0.014}$	1.08	1.227 ± 0.009		
N17	1.16	1.210 ± 0.010	1.00	$\mathbf{1.239 \pm 0.010}$	1.00	1.093 ± 0.007		
N18	1.09	1.172 ± 0.004	1.03	1.067 ± 0.006	1.05	1.221 ± 0.004	1.05	$\mathbf{1.241 \pm 0.005}$
N19	1.10	1.178 ± 0.003	1.15	1.141 ± 0.003	1.12	$\mathbf{1.271 \pm 0.008}$	1.12	$\mathbf{1.260 \pm 0.003}$
M-A	1.11	1.177 ± 0.036	1.17	1.158 ± 0.037	1.07	1.215 ± 0.025	1.08	1.263 ± 0.041
M-B		1.120 ± 0.031		1.066 ± 0.029		1.140 ± 0.021		1.182 ± 0.033
M-C		1.245 ± 0.066		1.223 ± 0.062		1.278 ± 0.05		1.308 ± 0.073

calculate the correlation coefficient and the P-values for testing the hypothesis that there is no inverse relationship between distance and temperature (null hypothesis). They are shown in Table 5, together with the slope $p1$ of a linear approximation:

$$T_B = p_1 \times d_{SM} + p_2 \tag{2}$$

Table 5 gives also the difference in brightness temperature as defined in Eq. (1) between two hypothetical measurements, where the Moon appeared with the same phase at low (8.18 min $\times$ c or $1.47{\cdot}10^8$ km) and high (8.44 min $\times$ c or $1.52{\cdot}10^8$ km) d_{SM} as calculated with Eq. (2). In the last column of Table 5 we compare our findings with the values predicted by Liu and Jin (2019) with a thermophysical model.

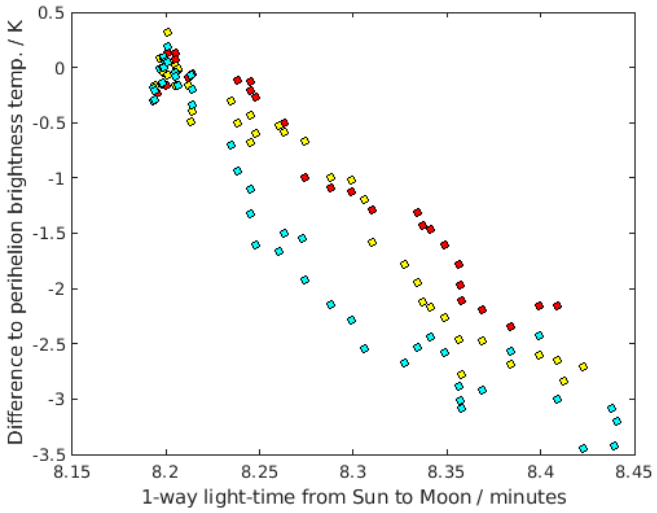

Figure 3. Disk-integrated brightness temperature of the Moon as a function of its distance to the Sun, expressed in light-minutes. The measurements were obtained with MHS on NOAA-18 at 89 GHz (channel 1, red), 157 GHz (channel 2, yellow), and 183/190 GHz (average of channels 3, 4, and 5, cyan). The closest the Moon can get to the Sun is a distance of 146,700,000 km or 8.155 light-min; the furthest point is at 152,500,000 km or 8.479 light-min. No Moon intrusions happened at these extreme points.

4.4 Brightness Temperature of the Waxing and Waning Moon

Based on our knowledge about the correct pointing direction and beamwidth of each channel and how to remove the effect of the varying distance between the Sun and the Moon, we can now calculate accurate, disk-integrated brightness temperatures of the Moon. The results are shown in Figure 4. The measured flux densities were normalised to the average distance of 8.3 min $\times$ c or $1.49 \cdot 10^8$ km between the Sun and the Moon, and only Moon intrusions that fulfilled the criteria for high reliability defined in Section 4.3 were considered. As channel 16 of AMSU-B and channel H1 of MHS have the best signal-to-noise ratios, we have at 89 GHz the largest and most reliable set of observations avail-

Table 5. Difference in Brightness Temperature Between Perihelion and Aphelion. The values in brackets are 95% confidence bounds.

Frequency (GHz)	R	P	p_1 (K/light-min)	ΔT_B^{MHS} (K)	ΔT_B^{Liu} (K)
89 (channel H1)	-0.3935	0.0031	-9.5 (-16.1, -2.8)	-2.5 (-4.2, -0.7)	-4.6
157 (channel H2)	-0.3718	0.0021	-13.0 (-21.7, -4.3)	-3.4 (-5.6, -1.1)	-5.2
183/190 (channel H3-5)	-0.4455	0.00025	-17.1 (-26.3, -7.9)	-4.4 (-6.8, -2.1)	-5.0

able for putting constraints on how the disk-integrated brightness temperature of the Moon varies with its phase angle. AMSU-B has larger noise than MHS at all frequencies (Hans et al., 2017), and that is why the scatter of the points from NOAA-16 and NOAA-17 is larger than that of other satellites. The measurements with channels H2 and 17, on the other hand, are the most problematic ones in our sample. The main reason for this is the fact that these channels correspond to different frequencies, and they have no exact analogue on ATMS either. Therefore the three instruments are here only comparable to some degree. Besides, we found a large scatter among the values obtained with channel 17 of AMSU-B on NOAA-16, and the ground tests produced a suspiciously high beam efficiency - 0.997 - for the space view of channel H2 on NOAA-18 (Costes, 1999). Therefore we excluded these satellites from Figure 4. We note that the channel at 165 GHz of ATMS was found to have by far the largest uncertainty in the study by Yang et al. (2020) as well. All sounding channels of AMSU-B and MHS provide the radiance of the Moon very close to 183.31 GHz with the exception of channel H5 on MHS, which operates at 190.31 GHz. Channel H3 on NOAA-19, however, was affected by radio-frequency interference, and the correction scheme by Hans et al. (2019) only works for Earth view counts. Therefore we excluded these data from our calculations and decided to plot the average of channels H4 and H5 in Figure 4 as a way to reduce the scatter of points. For consistency we included channel H5 also in the average values from MHS on NOAA-18. The scatter of the measurements with AMSU-B on NOAA-16 was again too high to allow a meaningful comparison with models of the lunar radiance. We also noted that for this instrument the uncertainty of the beam width of channels 17 - 20 was highest among the NOAA satellites, see Table 4, adding systematic to random uncertainty. All channels of AMSU-B on NOAA-15 experienced problems due to radio-frequency interference (Atkinson, 2001) as well, and therefore we calculated no brightness temperatures for the intrusions of the Moon in the DSV of this satellite.

5 Discussion

In order to demonstrate that our study is not just an academic exercise but provides concrete, new insights into the performance of microwave sounders in flight we compare the results from the ground tests of MHS by Matra Marconi / Airbus Defense & Space (Ackermann, 2018) to our Figure 2. The distance between the pointing directions on ground and in flight is in most cases less than 0.10° in the across track direction and less than 0.15° in the along track direction. If this additional pointing error in flight has the same direction as a considerable misalignment found already on ground, however, it produces a large absolute pointing error, i. e. a large difference between the nominal and the actual pointing direction. Its value in flight is given in the last column of Table 3. In several cases it does not agree with the findings on ground, resulting in clear violations of requirements, where at least marginal compliance had been claimed before. The most remarkable example is MHS on Metop-C, where according to Ackermann (2018) all channels are supposed to lie within 0.15°, corresponding to 2.1 km at nadir, of the nominal pointing direction, both in the along and the across track direction. The pro-

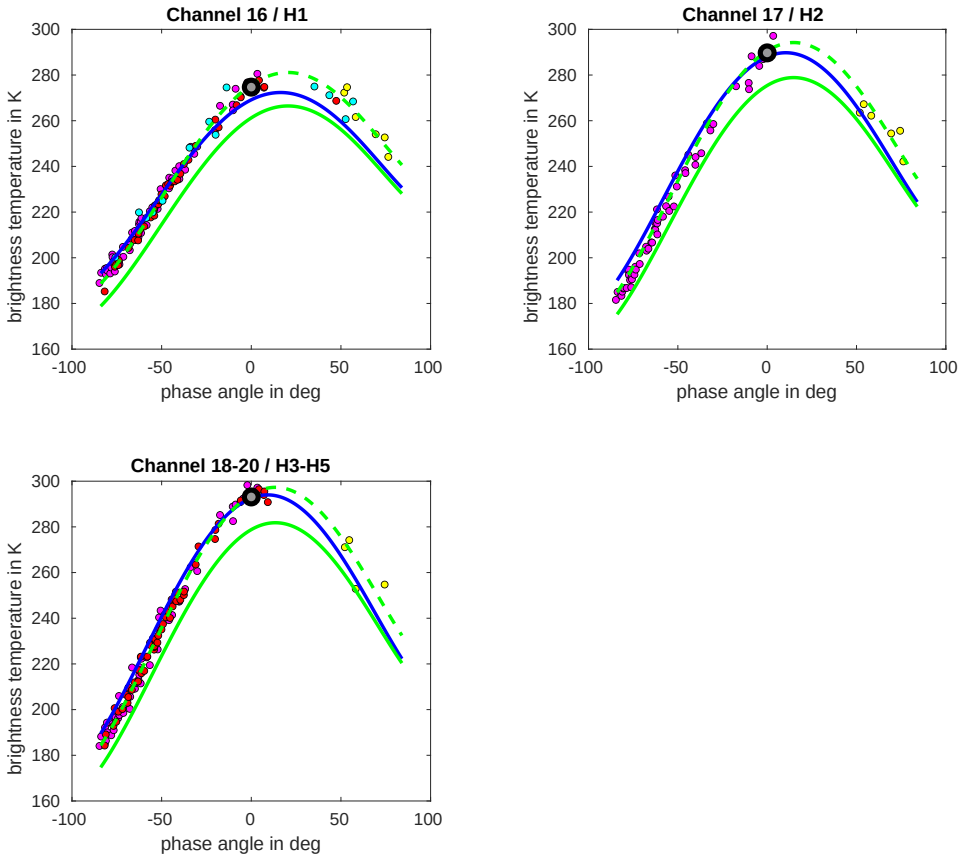

Figure 4. Brightness temperatures of the lunar disk from measurements at 89 GHz with AMSU-B on NOAA-16 (cyan) and NOAA-17 (yellow) and with MHS on NOAA-18 (red) and NOAA-19 (magenta), at 150 GHz with AMSU-B on NOAA-17 and at 157 GHz with MHS on NOAA-19, and as well with AMSU-B on NOAA-17 at 183.3 GHz and MHS on NOAA-18 and NOAA-19 with the average of the 183.3 and 190.3 GHz channels. The grey circle stands for ATMS on NOAA-20 (Yang et al., 2020) at the same frequencies, except for 165 GHz instead of 150 or 157 GHz. The blue line represents the brightness temperatures predicted by the model by Keihm (1984), the solid, green line represents the model by Liu and Jin (2020). The latter model has also been scaled to higher brightness temperatures with a factor 1.055, the result is shown as the dashed, green line.

gram "mhscl" in AAPP, however, located the Moon at least 0.39°, corresponding to 5.6 km at nadir, away from the position where it was actually found with MHS. After all a pointing error of this magnitude is more than the distance threshold criterion by John et al. (2012) for selecting collocations, viz. 5 km. Hence it is not possible to overcome spatial inhomogeneities, when simultaneous nadir overpasses are used for intercalibrating humidity sounding channels against MHS on Metop-C. It is important to realize that this offset between expected and actual position of the Moon is independent of the position of the spacecraft in orbit or the time of the year, i. e. the possibility that "mhscl" and "amsubcl" are at fault, for instance by calculating *systematically* wrong ephemerides for the Moon, can be ruled out. We also found pointing errors that violate the requirement for pointing accuracy by more than a factor of two with AMSU-B on NOAA-17, i. e. the last versions of AMSU-B and MHS have the worst pointing performance.

The situation is quite different, however, for the channels coregistration, i. e. the relative pointing error. Here we found compliance with the requirement of $\pm 0.07°$ for MHS (Costes, 1999) with almost all possible combinations of channels, as becomes apparent from the lines "H1 - H2" in Table 3. The coregistration was first determined with Moon intrusions by Bonsignori (2017), who focused on its component in the along-track direction for MHS on Metop-B. He found a small difference of 0.5 mrad or 0.029° between channels H1 and H2, where there was almost none in the ground tests. We confirmed Bonsignori's finding with our larger sample of measurements.

Bonsignori (2017) raised the question what might be the reason for the difference between the results on ground and in flight and identified three possible explanations, which are relevant for both absolute pointing and coregistration:

- errors in the ground measurement,
- errors in the in-orbit retrieval process,
- a genuine slight displacement of the components in the MHS quasi-optics.

The first explanation is difficult to prove many years after the fact. In particular the case of Metop-C, however, looks suspicious, because here the *absolute* pointing errors in either direction and of all channels turned out to be more than twice as big in flight as claimed by Airbus Defense & Space before launch. This is all the more surprising, since the accuracy of the results from the ground tests was claimed to be very good, viz. $\pm 0.01°$. The second explanation was ruled out by us repeating Bonsignori's investigation with many more intrusions of the Moon in the DSV and getting the same result. The last explanation requires strong forces acting on the instrument after the ground tests, and such forces were indeed present during the vibration test before launch and launch itself. They are probably the reason for the moderate anomaly of the pointing direction that Bonsignori (2017) detected with MHS on Metop-B.

Another crucial aspect of instrument performance in flight that can be addressed by analyzing intrusions of the Moon in the deep space view is the mean half power beamwidth. Again we found non-compliance; here the requirement is $1.1° \pm 10\%$ for both AMSU-B and MHS. It is not fulfilled for channel 17 of AMSU-B. For the sounding channels of MHS we find a beamwidth larger than 1.1° on all satellites, with Metop-C again having the largest deviation from the nominal value in all channels. The values for the beamwidth we obtained with Moon intrusions, however, had a much larger scatter with the Metop than with the NOAA satellites. As a consequence we got also much larger uncertainties for the mean beamwidth, see Table 4, and they suggest that the beam pattern of MHS on Metop differs considerably from the axisymmetric Gaussian we assumed for MHS on NOAA. As our calculation of the flux received from the Moon, however, relies on this assumption, we have not included the Metop satellites in our attempts to determine radiances and brightness temperatures.

With a strongly improved characterisation of the quasi-optical properties, we could set about calculating reliable, disk-integrated brightness temperatures of the Moon. Serendipitous observations of the Moon, i. e. those that are not carried out with dedicated maneuvers of the spacecraft, happen at different phase angles. It is therefore important to know exactly, how the radiance of the Moon depends on the phase angle, if one wants to establish the Moon as flux reference for microwave sounders. Another, more subtle effect, however, should not be neglected either: The dependence of the temperature of the Moon on its distance from the Sun. To our best knowledge this relationship has never been determined before directly from observations at the frequencies available to MHS, but there are recently published theoretical predictions (Liu & Jin, 2019). These differ from our findings chiefly with regard to their dependence on frequency: The difference between T_B at perihelion and aphelion is according to the model at 89 GHz only 0.4 K smaller than at 183 GHz. According to our measurements with MHS, however, this dif-

ference amounts to 1.9 K, and the temperature changes are most pronounced at 183 GHz, not at 157 GHz, as postulated by Liu and Jin (2019). But our measurements have a rather large uncertainty, so a larger data set is needed to clarify the situation.

If the varying distance between the Sun and the Moon was not taken into account, then the calculated brightness temperatures of the Moon would be more uncertain. This uncertainty has a strong, systematic component, because 42 intrusions of the Moon in our sample from NOAA-18, for example, happened in January, but none in July. This caused the high number of points at low distance between the Moon and the Sun in Figure 3. Even worse, this imbalance between Moon intrusions near and far from the Sun changes with time: Only one quarter of the Moon intrusions in January happened in the second half of the operational lifetime of the instrument. This means that a correction for the solar distance effect is essential for checking the photometric stability of an instrument with the Moon. It is also relevant for the relationship between measured brightness temperature and phase angle, because the phase angle of the Moon intrusions changes over the years as well, unless the equator crossing time is kept constant. As the solar distance effect is rather small, we repeated our investigation with MHS on another satelite, namely NOAA-19. We obtained similar results, albeit with larger random uncertainties.

Applying strict selection criteria resulted in a set of about 50 intrusions of the Moon in the DSV of MHS on both NOAA-18 and -19, two instruments that combine low noise in most channels with Moon intrusions over a rather large range of phase angles. Comparing their brightness temperatures with model predictions, and adding some values from AMSU-B on NOAA-17, which observed the waning Moon, we could provide additional evidence for the claim by Burgdorf et al. (2019) that the model by Keihm (1984) does not reflect correctly the difference in brightness temperature between waxing and waning Moon and the phase angle of maximum disk-integrated brightness temperature. In order to quantify the comparison between observation and models, we have calculated the difference between the measured brightness temperature of the Moon and the predictions of the models - Keihm's, Liu's, and a polynomial of fifth order fitted to the measurements - for all points obtained with channel 1 of MHS on NOAA-18. The mean of these differences indicates how well the models reproduce the absolute radiance level of the Moon, whereas the standard deviation of these values depends on the noise of the measurements but also on how well the models reproduce the dependence of disk-integrated flux density on the phase angle. The standard deviation was 2.02 K both with Liu's model and the polynomial fitted to the data themselves, whereas it was 3.52 K with Keihm's model. This shows that Liu's model fits the changes of the measured brightness temperature of the Moon as a function of phase angle extremely well. All that is needed to bring the model by Liu and Jin (2020) in complete agreement with the measurements at the different frequencies, is to scale up its brightness temperatures by a factor 1.055. The shape of the function that describes the changes of radiance with phase angle, however, is already sufficient to make measurements from different Moon intrusions comparable. Therefore we are confident that the model by Liu and Jin (2020) will prove to be quite helpful for future studies in inter-calibration and photometric stability of microwave sounders. But what causes this model to give brightness temperatures for full Moon that are more than 10 K lower than the measured values or those predicted by Keihm (1984)? Obviously every model needs accurate input values for the surface temperature and other thermophysical parameters. Liu and Jin (2020) relied for this amongst other things on the Diviner data of the Lunar Reconnaissance Orbiter (Vasavada et al., 2012), even though the calibration of this instrument was still being worked on (Aye, 2019) at the time. It will be interesting to see, whether the final Diviner re-calibration will eventually result in higher surface temperatures.

6 Conclusions

With our study of intrusions of the Moon in the deep space view of several microwave sounders we have demonstrated how these events can provide information about the performance of the instruments that is impossible to obtain any other way. This is true in particular for the pointing error of the sounding channels, because their quasi-optical path is different from the other channels, and one cannot identify landmarks in their scans. We provide a compilation of the most important properties of the quasi-optics for all AMSU-B and MHS in orbit, which can serve as a reference that facilitates the comparison between different instruments. Finally we could demonstrate that inter-calibration between any pair of microwave sounders is now possible by analyzing the intrusions of the Moon in the DSV and eliminating the effects of the relative positions of Earth, Moon, and Sun.

Acknowledgments

The authors would like to thank Niklas Anczykowski for his analysis of intrusions of the Moon in the deep space views of microwave sounders. The authors would like to thank Tim Hewison and Cheng-Zhi Zou for contributing questions to be addressed in this manuscript.

This research was funded by Deutsche Forschungsgemeinschaft, project number 421761264 (MW-Luna). With this work we contribute to the Cluster of Excellence "CLICCS—Climate, Climatic Change, and Society" funded by the Deutsche Forschungsgemeinschaft DFG (EXC 2037, Project Number 390683824), and to the Center for Earth System Research and Sustainability (CEN) of Universität Hamburg.

The raw data from the spacecrafts mentioned in this article are supplied by the NOAA Comprehensive Large Array-data Stewardship System.

References

Ackermann, J. (2018). Pointing accuracy and co-alignment. *EUMETSAT website*. Retrieved from `https://www.eumetsat.int/website/home/Satellites/CurrentSatellites/Metop/MetopDesign/MHS/index.html`

Appel, J. W., Xu, Z., Padilla, I. L., Harrington, K., Pradenas Marquez, B., Ali, A., ... Zeng, L. (2019, May). On-sky performance of the class q-band telescope. *The Astrophysical Journal*, *876*(2), 126. doi: 10.3847/1538-4357/ab1652

Atkinson, N. (2001). Calibration, monitoring and validation of amsu-b. *Advances in Space Research*, *28*(1), 117 - 126. Retrieved from `http://www.sciencedirect.com/science/article/pii/S027311770100312X` doi: https://doi.org/10.1016/S0273-1177(01)00312-X

Aye, K.-M. (2019, March). LRO Diviner Re-Calibration and Its Effect on Volatile Research. In *Lunar and planetary science conference* (p. 3259).

Bonsignori, R. (2017). In-orbit verification of mhs spectral channels co-registration using the moon. In J. J. Butler, X. J. Xiong, & X. Gu (Eds.), *Earth observing systems xxii* (Vol. 10402, pp. 714 – 722). SPIE. Retrieved from `https://doi.org/10.1117/12.2273335` doi: 10.1117/12.2273335

Burgdorf, M., Buehler, S. A., Hans, I., & Prange, M. (2019). Disk-integrated lunar brightness temperatures between 89 and 190 ghz. *Advances in Astronomy*, *2019*. Retrieved from `https://doi.org/10.1155/2019/2350476` doi: 10.1155/2019/2350476

Burgdorf, M., Lang, T., Michel, S., Buehler, S. A., & Hans, I. (2016). The moon as a diagnostic tool for microwave sensors. *GSICS Quarterly Newsletters*, *10*. Retrieved from `https://repository.library.noaa.gov/view/noaa/17928` doi: 10.7289/V5GT5K7S

Costes, L. (1998). Microwave humidity sounder fm2 antenna test report. In

C. Whatling (Ed.), *Microwave humidity sounder instrument end item data package fm2 model* (Vol. 3, p. 162).

Costes, L. (1999). Microwave humidity sounder pfm antenna test report. In C. Whatling (Ed.), *Microwave humidity sounder instrument end item data package pfm model* (Vol. 3, p. 134).

Costes, L., Bushell, C., Buckley, M. J., & Mason, G. (1999). Microwave Humidity Sounder (MHS) antenna. In H. Fujisada & J. B. Lurie (Eds.), *Sensors, systems, and next-generation satellites iii* (Vol. 3870, pp. 412 – 426). SPIE. Retrieved from https://doi.org/10.1117/12.373211 doi: 10.1117/12.373211

EUMETSAT. (2013). Mhs level 1 product generation specification. *EUMETSAT website*. Retrieved from https://www-cdn.eumetsat.int/files/2020-04/pdf_ten_990006-eps-mhs-l1-pgs.pdf

Hans, I., Burgdorf, M., & Buehler, S. A. (2019, Apr). Onboard radio frequency interference as the origin of inter-satellite biases for microwave humidity sounders. *Remote Sensing*, *11*(7), 866. Retrieved from http://dx.doi.org/10.3390/rs11070866 doi: 10.3390/rs11070866

Hans, I., Burgdorf, M., John, V. O., Mittaz, J., & Buehler, S. A. (2017). Noise performance of microwave humidity sounders over their lifetime. *Atmospheric Measurement Techniques*, *10*(12), 4927–4945. Retrieved from https://amt.copernicus.org/articles/10/4927/2017/ doi: 10.5194/amt-10-4927-2017

Hewison, T. J. (1993). Amsu-b antenna test results. In *Met o branch technical note* (Vol. No. 2, p. 68). Remote Sensing Instrumentation Branch.

John, V. O., Holl, G., Buehler, S. A., Candy, B., Saunders, R. W., & Parker, D. E. (2012, January). Understanding intersatellite biases of microwave humidity sounders using global simultaneous nadir overpasses. *Journal of Geophysical Research (Atmospheres)*, *117*(D2), D02305. doi: 10.1029/2011JD016349

Keihm, S. J. (1984). Interpretation of the lunar microwave brightness temperature spectrum: Feasibility of orbital heat flow mapping. *Icarus*, *60*(3), 568 - 589. Retrieved from http://www.sciencedirect.com/science/article/pii/0019103584901659 doi: https://doi.org/10.1016/0019-1035(84)90165-9

Kieffer, H. H., & Stone, T. C. (2005, jun). The spectral irradiance of the moon. *The Astronomical Journal*, *129*(6), 2887–2901. Retrieved from https://doi.org/10.1086%2F430185 doi: 10.1086/430185

Kieffer, H. H., Stone, T. C., Barnes, R. A., Bender, S. C., Jr., R. E. E., Mendenhall, J. A., & Ong, L. (2003). On-orbit radiometric calibration over time and between spacecraft using the Moon. In H. Fujisada et al. (Eds.), *Sensors, systems, and next-generation satellites vi* (Vol. 4881, pp. 287 – 298). SPIE. Retrieved from https://doi.org/10.1117/12.462611 doi: 10.1117/12.462611

Kouyama, T., Yokota, Y., Ishihara, Y., Nakamura, R., Yamamoto, S., & Matsunaga, T. (2016). Development of an application scheme for the selene/sp lunar reflectance model for radiometric calibration of hyperspectral and multispectral sensors. *Planetary and Space Science*, *124*, 76 - 83. Retrieved from http://www.sciencedirect.com/science/article/pii/S0032063315301008 doi: https://doi.org/10.1016/j.pss.2016.02.003

Krotikov, V. D., & Pelyushenko, S. A. (1987, April). The problem of using the moon as source with a reference intensity in the 0.1-30 CM wavelength range. *Soviet Astronomy*, *64*, 417-423.

Liu, N., & Jin, Y. (2019). Calibration of a multichannel millimeter wave radiometer of fy-4m based on the real-time brightness temperature along the lunar equator. *Chin Sci Bull*, *64*, 1-9.

Liu, N., & Jin, Y. (2020). Average brightness temperature of lunar surface for calibration of multichannel millimeter-wave radiometer from 89 to 183 ghz and data validation. *IEEE Transactions on Geoscience and Remote Sensing*, 1-10.

Moradi, I., Meng, H., Ferraro, R. R., & Bilanow, S. (2013, jun). Correcting geolo-

cation errors for microwave instruments aboard noaa satellites. *IEEE Transactions on Geoscience and Remote Sensing*, *51*(6), 3625-3637. doi: 10.1109/TGRS.2012.2225840

Robel, J., & Graumann, A. (2014). Noaa klm user's guide. National Environmental Satellite, Data, and Information Service. Retrieved from `https://archive.org/details/noaa-klm-guide/mode/2up`

Stone, T. C. (2010). Stellar calibration of the ROLO lunar radiometric reference. In J. J. Butler, X. Xiong, & X. Gu (Eds.), *Earth observing systems xv* (Vol. 7807, pp. 226 – 235). SPIE. Retrieved from `https://doi.org/10.1117/12.862141` doi: 10.1117/12.862141

Vasavada, A. R., Bandfield, J. L., Greenhagen, B. T., Hayne, P. O., Siegler, M. A., Williams, J.-P., & Paige, D. A. (2012). Lunar equatorial surface temperatures and regolith properties from the diviner lunar radiometer experiment. *Journal of Geophysical Research: Planets*, *117*(E12). Retrieved from `https://agupubs.onlinelibrary.wiley.com/doi/abs/10.1029/2011JE003987` doi: https://doi.org/10.1029/2011JE003987

Xu, Z., Brewer, M., Rojas, P. F., Li, Y., Osumi, K., Pradenas, B., ... Wollack, E. J. (2020). Two-year cosmology large angular scale surveyor (class) observations. *Astrophysical Journal*, *891*(134), 25.

Yang, H., & Burgdorf, M. (2020, April). A Study of Lunar Microwave Radiation Based on Satellite Observations. *Remote Sensing*, *12*(7), 1129. doi: 10.3390/rs12071129

Yang, H., Zhou, J., Sun, N., Liu, Q., Leslie, R., Anderson, K., ... McCormick, L. (2020). 2-d lunar microwave radiance observations from the noaa-20 atms. *IEEE Geoscience and Remote Sensing Letters*, 1-4.